Light-sheet 3D microprinting via two-colour two-step absorption

Vincent Hahn[1,2] ✉, Pascal Rietz[1,2], Frank Hermann[1], Patrick Müller[2,3], Christopher Barner-Kowollik[2,4], Tobias Schlöder[2], Wolfgang Wenzel[2], Eva Blasco[5,6] and Martin Wegener[1,2]

High-speed high-resolution 3D printing of polymers is highly desirable for many applications, yet still technologically challenging. Today, optics-based printing is in the lead. Projection-based linear optical approaches have achieved high printing rates of around 10^6 voxels s^{-1}, although at voxel volumes of >100 µm^3. Scanning-based nonlinear optical approaches have achieved voxel volumes of <1 µm^3, but suffer from low printing speed or high cost because of the required femtosecond lasers. Here we present an approach that we refer to as light-sheet 3D laser microprinting. It combines image projection with an AND-type optical nonlinearity based on two-colour two-step absorption. The underlying photoresin is composed of 2,3-butanedione as the photoinitiator, (2,2,6,6-tetramethylpiperidin-1-yl)oxyl as the scavenger and dipentaerythritol hexaacrylate as the multifunctional monomer. Using continuous-wave laser diodes at 440 nm wavelength for projection and a continuous-wave laser at 660 nm for the light-sheet, we achieve a peak printing rate of 7×10^6 voxels s^{-1} at a voxel volume of 0.55 µm^3.

The dream of three-dimensional (3D) additive manufacturing is to manufacture complex 3D (polymer) parts more flexibly, with higher precision, faster and more cost economic than well-established technologies such as, for example, injection moulding. Today, 3D printing is already more flexible because no casts are needed. Although milling of casts has reached micrometre precision[1], formative and subtractive manufacturing processes impose constraints on the fabricated geometries that are not faced in 3D printing[1]. Also, 3D printing has long reached the sub-micrometre scale, which is not easily possible otherwise. However, in injection moulding, typical fabrication times per part are on the order of a few seconds. As emphasized in the 2018 review on 3D additive manufacturing[2], current 3D printers are substantially slower. This slowness is clearly connected to higher manufacturing costs, making the increase in 3D printing speed a major—if not the major challenge—in the field of 3D additive manufacturing.

Among the emerging 3D printing technologies aspiring to speed up the printing rates compared with well-established projection micro-stereolithography[3,4] are computed axial lithography (CAL)[5–7], continuous liquid interface production (CLIP)[8–10], rapid-scanning multifocus multiphoton 3D laser printing (MFMP-3DP)[11–13], femtosecond projection two-photon lithography (FP-TPL)[14,15], and light-sheet 3D printing[16], later also called xolography[17]. In all these approaches, a liquid photoresin is solidified under irradiation with light. For CAL, the photoresin is cured via one-photon absorption, that is, using blue or ultraviolet (UV) light, by sequentially exposing the photoresist to pre-calculated images from multiple directions. The photoresin solidifies only at locations where sufficient dose has accumulated. The consequently attained minimum voxel volumes are larger than 5×10^5 µm^3. Using CLIP, similar voxel volumes are achieved by curing layers of a highly absorbing photoresin, again via one-photon absorption. In both

[1]Institute of Applied Physics, Karlsruhe Institute of Technology (KIT), Karlsruhe, Germany. [2]Institute of Nanotechnology, Karlsruhe Institute of Technology (KIT), Karlsruhe, Germany. [3]Nanoscribe GmbH & Co. KG, Eggenstein-Leopoldshafen, Germany. [4]Centre for Materials Science, School of Chemistry and Physics, Queensland University of Technology (QUT), Brisbane, Queensland, Australia. [5]Institute for Molecular Systems Engineering and Advanced Materials, Ruprecht-Karls-Universität Heidelberg, Heidelberg, Germany. [6]Institute of Organic Chemistry, Ruprecht-Karls-Universität Heidelberg, Heidelberg, Germany. ✉e-mail: vincent.hahn@kit.edu

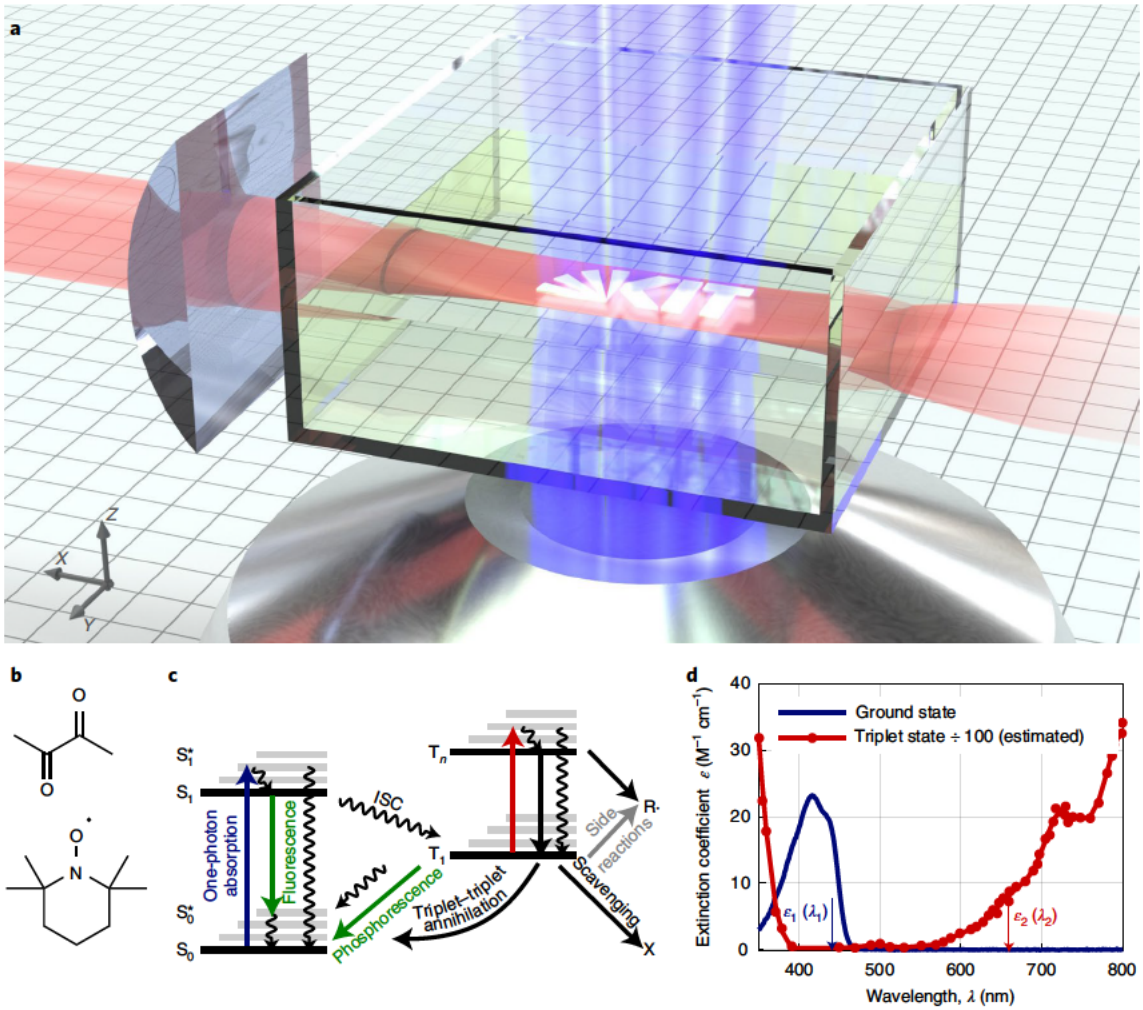

Fig. 1 | Light-sheet 3D printing via non-degenerate two-step absorption photoinitiation. a, Artistic rendered sketch of the light-sheet 3D printing process. The red light-sheet is focused by cylindrical optics into the transparent cuvette filled with a yellow-tinted photoresin. The blue projection beam is focused by a high-NA microscope objective lens (bottom) and intersects the light-sheet beam in the focal plane. At this intersection, the liquid photoresin polymerizes in the shape of the projected Karlsruhe Institute of Technology (KIT) logo. 3D objects are printed by scanning along the *z* direction. **b**, Photoinitiator molecule biacetyl (top) and TEMPO (bottom), a radical scavenger and triplet quencher. **c**, Jablonski diagram of biacetyl. Molecules in the singlet ground state S_0 can be excited by blue light to an excited singlet state S_1. From there, molecules mainly undergo intersystem crossing (ISC), leading to a population of the triplet ground state T_1. This state naturally decays into the singlet ground state S_0, for example, by emitting phosphorescence[46]. Additionally, solvated oxygen, TEMPO, the monomer and other biacetyl molecules in their triplet state quench the T_1 population. We have found that TEMPO also suppresses unwanted side reactions emerging from this state. Finally, molecules in the T_1 state can be re-excited by red or UV light to an excited triplet state, from which biacetyl can decay into free radicals, initiating a polymerization reaction. **d**, Measured ground-state extinction spectrum for biacetyl (dark blue) and estimated triplet-state extinction spectrum (red). The latter is scaled by a factor of 100 from the data taken from the literature[26,47].

MFMP-3DP and FP-TPL, light is absorbed via two-photon or multiphoton absorption. In MFMP-3DLP, for example, as many as nine laser foci were scanned in parallel at a focus speed of about 0.5 m s^{-1} (ref. [13]). In FP-TPL, a light pattern (for example, a line) in one layer is even scanned at a considerable fraction of the speed of light[18,19]. Therefore, for both approaches, bulky and expensive high-power femtosecond lasers are needed. The laser power and cost increase with the printing speed. This scaling is unfortunate and may ultimately limit further progress along these lines.

Here we introduce a light-sheet 3D printing photoresin system and a light-sheet 3D printing setup, the combination of which is capable of printing voxels with lateral sizes of 0.5 µm and volumes of 0.55 $µm^3$ at a peak printing rate of 7×10^6 voxels s^{-1}. This novel approach can be seen as a parallelization of one-colour two-step absorption, which uses a low-power continuous-wave laser for focus-scanning 3D laser nanoprinting[20]. In this work, we employ two-colour two-step absorption using biacetyl as the photoinitiator. With this logical-AND optical gate, chemical reactions are only triggered at locations where the continuous-wave light-sheet laser emitting at 660 nm wavelength and the continuous-wave projection laser at 440 nm have a sufficiently large intensity. We demonstrate the resolution and throughput capabilities of our light-sheet approach by 3D printing suspended line gratings, 3D metamaterial crystals and various other standard 3D test structures. Importantly, the typical overall printing time per part is below 1 s.

Figure 1a illustrates the light-sheet 3D printing process. A liquid photoresin is exposed layer by layer by projecting slices of a 3D object using light of wavelength λ_1 (blue). To avoid polymerization of the liquid resin along the entire optical axis, the photoresin is designed such that it solidifies only in locations that are simultaneously exposed by a light beam of another wavelength, namely, λ_2 (red). Therefore, a light-sheet beam is used. It is formed using a cylindrical lens that tightly focuses the beam only along one axis. The plane of the light-sheet and focal plane of the projected image are superimposed. In this configuration, in regions above and below the focal plane, no polymerization reaction is triggered, that is, a negligible dose is accumulated.

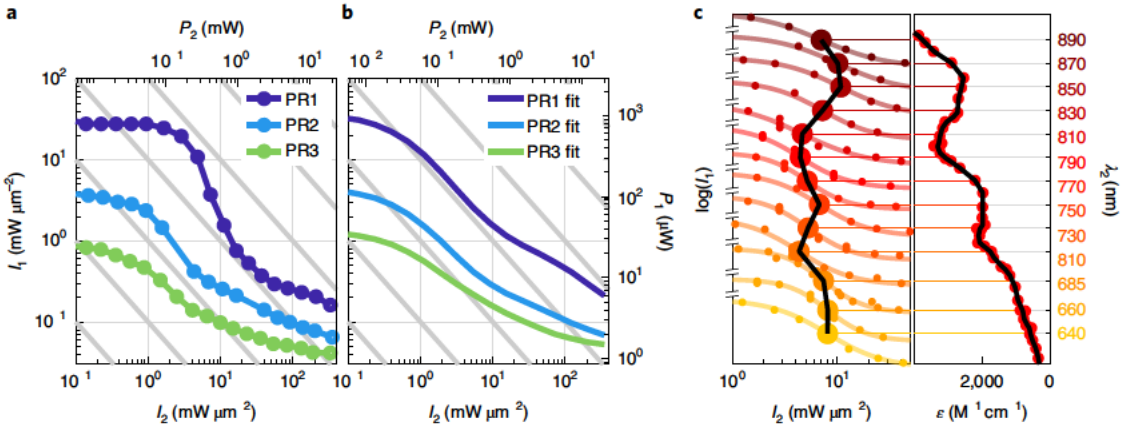

Fig. 2 | Two-colour point-scanning polymerization threshold experiments on biacetyl-containing photoresins. a, Two-colour point-scanning-exposure polymerization threshold experiments for three different photoresins (PR1–PR3), containing monomers of different viscosities. For increasing red laser intensity (I_2), the necessary blue laser intensity (I_1), at which the monomer is sufficiently crosslinked to form a solid polymer network, decreases. This effect is the most pronounced for the least viscous monomer, namely, trimethylolpropane triacrylate (TMPTA). Additional results of the point-scanning experiments are shown in Supplementary Figs. 6–8. **b**, Results of rate model calculations corresponding to the experiments shown in **a**. The curves qualitatively reproduce the experimental observations. Details on the calculations are provided in Supplementary Note 1. **c**, Stacked plot of two-colour point-scanning exposure experiments for photoresin PR1 using different red laser wavelengths λ_2. A logistic function is fitted to each experiment (not all the fitted data points fall within the plotted range). The sigmoid midpoint values are highlighted and outlined by the black curve. This curve can be compared with the triplet–triplet absorption spectrum of biacetyl (right). The triplet–triplet absorption data are extracted from elsewhere[26] (Fig. 1d). The black curve in **c** (right) is a smoothing spline curve through the red data points.

Results

Two-colour two-step photoinitiation

The key ingredient of the photoresin is the photoinitiator. Upon absorption of light of wavelength λ_1, it enters an idle intermediate electronic state, from which the photoinitiator naturally decays back into its ground state. However, if the pre-excited idle photoinitiator absorbs a photon of wavelength λ_2, the molecule is further excited to an energetically higher state from which the polymerization reaction is initiated. The polymerization reaction crosslinks the liquid monomer, for example, by photoinitiator molecules fragmenting into free radicals. We refer to this process as two-colour two-step absorption. It is illustrated by an electron state diagram (Fig. 1c). Importantly, continuous-wave lasers can be used for both colours.

A good photoinitiator for light-sheet 3D printing must fulfil several criteria. First and foremost, one wants to avoid the case that light of either wavelength, λ_1 or λ_2, alone is able to promote both transitions in the photoinitiator and thereby triggering the polymerization reaction, which would result in an undesired crosslinking of the photoresin. Therefore, it is vital that the two-step absorption spectra of the ground and intermediate state contain non-overlapping regions (that is, the transitions are not degenerate). The two wavelengths are chosen such that the photoinitiator in its ground (intermediate) state does not absorb light of wavelength λ_2 (λ_1). Note that this choice is the polar opposite of what we have used in laser-scanning one-colour two-step absorption 3D nanoprinting[20], where one wavelength is intentionally chosen to trigger both optical transitions.

However, this criterion alone is not sufficient for a good two-colour two-step photoinitiator. A second crucial condition is that the photoinitiator molecule in its intermediate state decays back to the ground state in due time. Suppose this criterion is not fulfilled: after exposure of the first layer, the photoinitiator molecules along the entire optical path are promoted by light at wavelength λ_1 to the intermediate state—and remain there, even after progressing with the exposure to the next layer. In this layer, exposure with the light-sheet (at wavelength λ_2) alone suffices to polymerize the previous slice pattern in the photoresin. Hence, when exposing subsequent layers, one has to wait for the pre-excited photoinitiator molecules of the previously exposed layer to decay back to the ground state. This waiting time is governed by the intermediate-state lifetime and ultimately limits either the achievable printing rate or the spatial resolution.

The third criterion may appear somewhat counterintuitive at first sight. The photoinitiator's ground-state extinction coefficient at wavelength λ_1 must be sufficiently low, such that a large enough intensity is transmitted to the focal plane. For example, typical photoresins contain photoinitiator concentrations in the range of 1% (wt.%) or about 20 mM (assuming a photoinitiator molar weight of 500 g mol^{-1} and a mass density of 1 g ml^{-1}). Furthermore, assuming a molar decadic extinction coefficient of 1,000 M^{-1} cm^{-1} and a free-working distance of the projecting microscope objective lens of 500 µm, the light intensity would decay by an order of magnitude to 10% of the incident intensity via Beer's law, which is clearly not acceptable.

Table 1 | Photoresin compositions used for the experiments

Name	Monomer	[BA]	[TEMPO]	Viscosity
PR1	TMPTA	0.11 M (1.1 wt.%)	0.011 M (0.2 wt.%)	0.1 PaS
PR2	PETA	0.11 M (1.1 wt.%)	0.011 M (0.2 wt.%)	1.0 PaS
PR3	DPEHA	0.11 M (1.1 wt.%)	0.011 M (0.2 wt.%)	6.0 PaS

Abbreviations: TMPTA, trimethylolpropane triacrylate; PETA, pentaerythritol triacrylate; DPEHA, dipentaerythritol hexaacrylate; TEMPO, (2,2,6,6-tetramethylpiperidin-1-yl)oxyl; BA, biacetyl. At room temperature, DPEHA solidifies by forming crystallites within the course of a few weeks. Therefore, DPEHA is stirred on a hotplate at a temperature of 45 °C until crystallites are completely dissolved, before adding further ingredients to the photoresin. After adding TEMPO, the photoresins PR1–PR3 are stirred at a temperature of 45 °C until TEMPO is completely dissolved. PR1 and PR2 are stirred for 1h at room temperature after adding biacetyl. PR3 is stirred for 1h on a hotplate at a temperature of 45 °C after adding biacetyl. The viscosities at the temperature of 25 °C are taken from the vendor's certificate of analysis, except for the viscosity of PETA, which is measured at a temperature of 20 °C and taken from another work[45].

Biacetyl and TEMPO as the photoinitiator system

A photoinitiator molecule that fulfils these three criteria is 2,3-butanedione, commonly known as diacetyl or biacetyl (Fig. 1b, top). A corresponding Jablonski diagram for biacetyl is shown in Fig. 1c. Upon absorption of a blue photon, the molecule is excited from

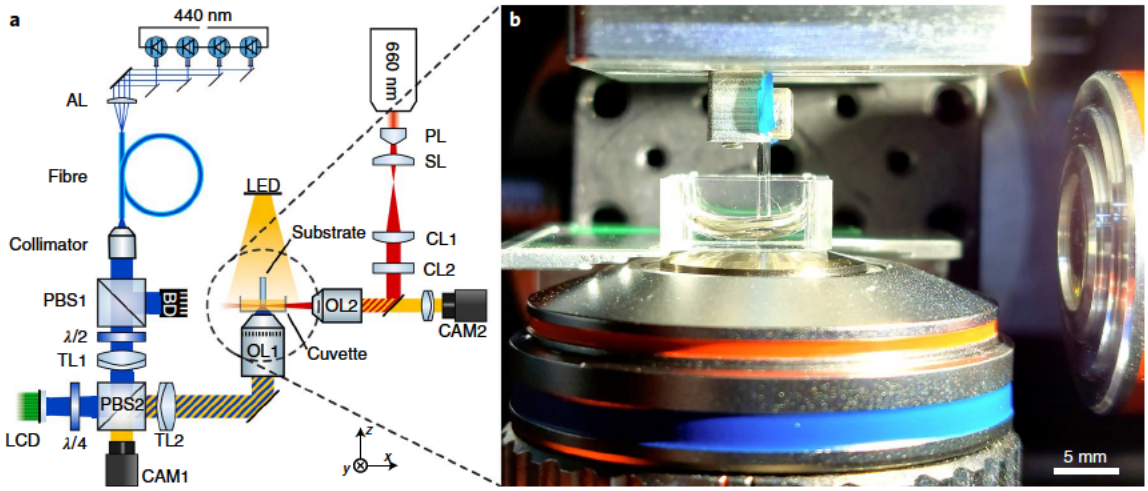

Fig. 3 | Light-sheet 3D printing setup. a, Sketch of the light-sheet 3D printing setup. AL, aspheric lens; PBS, polarizing beamsplitter; BD, beam dump; TL, tube lens; LCD, liquid-crystal display; CAM, camera; OL, objective lens; LED, light-emitting diode; CL, cylindrical lens; SL, spherical lens; PL, Powell lens. The detailed component lists are provided in the Methods section and Supplementary Tables 2 and 3. **b**, Photograph of the 3D printing glass-rod substrate, dipped into the cuvette. Below the cuvette, the projection objective lens is mounted. On the right-hand side, the light-sheet microscope objective lens can be seen.

the singlet ground state S_0 to an excited state S_1 and undergoes efficient intersystem crossing (99.8% quantum yield) to the triplet ground state T_1 (ref. [21]). Biacetyl's triplet ground-state energy of 235 kJ mol^{-1} (2.44 eV) is relatively low[22–24] compared with other photoinitiators[25] and lower than typical bond-cleavage energies of 293 kJ mol^{-1} (ref. [26]). Hence, biacetyl cannot efficiently fragment into radicals from its T_1 state. However, starting from the T_1 state, using light in the UV, red, and near-infrared regions[26], biacetyl can be optically excited to energetically higher states. The corresponding excited-state absorption spectrum is also plotted in Fig. 1d. In the excited triplet state, biacetyl has sufficient energy to fragment into radicals.

For all our experiments, we choose $\lambda_1 = 440$ nm. For the point-scanning pre-experiments, we use $\lambda_2 = 640$ nm (unless stated otherwise); for the light-sheet 3D printing experiments, $\lambda_2 = 660$ nm, where high-power solid-state laser sources are readily available. As evident from Fig. 1d, there is no overlap in the absorption spectra at the pair of wavelengths (λ_1 and λ_2) and hence the first criterion for a good light-sheet photoinitiator is fulfilled. The intermediate-state lifetime, that is, the triplet state in the case of biacetyl, was measured in degassed solutions and is on the order of 100 µs (ref. [27]), equivalent to a decay rate of 10^4 s^{-1}. Since this rate is faster than the frame rate of available projectors and thus does not restrict the printing rate, the second criterion is met, too. Moreover, ingredients within the photoresin can act as a triplet quencher and further reduce the triplet lifetime[28–31]. We will address the intermediate-state lifetime in the photoresin below, by comparison of the experimental data with rate equation calculations. Finally, at $\lambda_1 = 440$ nm, the molar decadic extinction coefficient in acetonitrile is 18 M^{-1} cm^{-1}. With the used photoinitiator concentration of 110 mM and a microscope-lens free-working distance of 500 µm, the intensity in the focal plane only decays to about 80% of the incident intensity. Therefore, biacetyl also fulfils the third criterion.

However, similar to most ketones[24], biacetyl in its triplet ground state can abstract a hydrogen atom from nearby susceptible groups[24]. Furthermore, thermally activated bond cleavage[32] and reactions with oxygen[33] are possible decay mechanisms. These reactions potentially result in radicals being formed from the intermediate state. This behaviour is clearly undesired, as it would lead to the polymerization of photoresin triggered by light of only one wavelength, that is, λ_1. To suppress such unwanted side reactions, we introduce (2,2,6,6-tetramethylpiperidin-1-yl)oxyl (TEMPO) to the photoresin (Fig. 1b, bottom). TEMPO is a persistent radical and belongs to the group of hindered amine light stabilizers[34]. It acts as a radical scavenger[35] and serves as a triplet-state quencher[30]. In our experiments, we found that TEMPO efficiently suppresses polymerization triggered by only light of wavelength λ_1 under suitable conditions. We now quantify this aspect.

For our characterization experiments, we used three different photoresins PR1–PR3 (Table 1). The photoresins contain acrylate monomers of different viscosities and degrees of functionalization. We measured the polymerization threshold laser intensity of the photoresins by co-focusing two laser beams of wavelength $\lambda_1 = 440$ nm (blue) and $\lambda_2 = 640$ nm (red) through a large-numerical-aperture (NA = 1.4) objective lens into the photoresin and printing dashed-line patterns at a constant focus velocity of $v_0 = 100$ µm s^{-1}. The blue and red laser intensities are independently varied. For each red laser intensity I_2, we record the minimal blue laser intensity I_1 that leads to an optically visible polymerized line after sample development. This point marks the polymerization threshold. In Fig. 2a, we plot I_1 versus I_2 in a two-colour polymerization-threshold diagram on a double-logarithmic scale. On the right-hand-side vertical axis (Fig. 2b), the blue laser intensity is converted to blue power by using the measured full-width at half-maximum of the focus diameter of the blue laser. On the upper horizontal axis (Fig. 2b), the corresponding power for the red laser is given, similarly obtained from the full-width at half-maximum of the focus diameter of the red laser. The intensity scales allow for a direct comparison with the below light-sheet printing experiments. As evident from the figure, for zero and low red laser powers, the blue-laser threshold power is around $P_1(P_2 = 0\ \text{mW}) = 0.9$ mW (corresponding to an intensity of 31 mW µm^{-2}) for photoresin PR1. With increasing red laser power, the blue-laser polymerization threshold decreases in a sigmoid fashion and plateaus at about $P_1(P_2 = 20\ \text{mW}) = 4.6$ µW (corresponding to an intensity of 0.16 mW µm^{-2}). Hence, the two-colour polymerization contrast, which we define as the ratio of the two blue-laser threshold powers, is as large as about 200, consistent with the expectation for a good two-colour two-step absorption process. Ideally, this ratio should be infinitely large. The measured polymerization threshold intensities are in good agreement with the results of rate equation calculations (Fig. 2b). The rate model with an intermediate-state lifetime of <200 µs is discussed in detail in Supplementary Note 1.

To further test the two-colour two-step absorption behaviour, we repeated the threshold power experiments for a set of red laser wavelengths λ_2, ranging from 640 to 890 nm. Figure 2c (left) shows the corresponding vertically stacked two-colour polymerization threshold

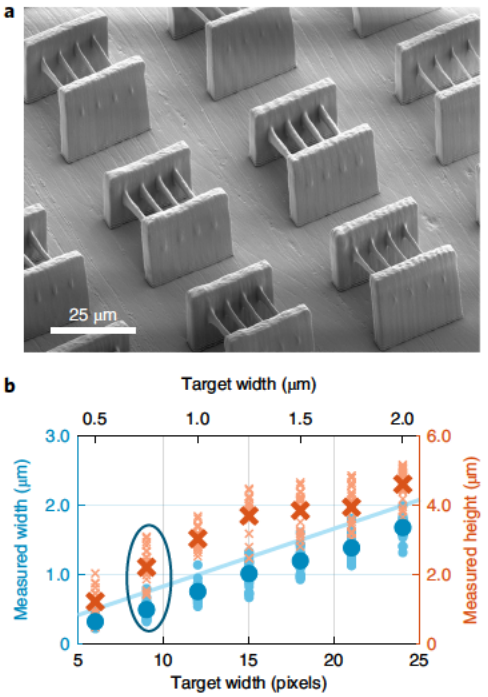

Fig. 4 | Suspended lines as 3D printing voxel-size benchmark. a, SEM image of a series of suspended lines with a pitch of 6 µm and length of 20 µm. The exposure time for each line grating was fixed at 5 ms. The blue laser intensity in the focal plane was $I_1 = 160\ \mu W\ \mu m^{-2}$, and the red laser power was set to $P_2 = 3$ W to avoid possible saturation effects. During the exposure of lines, all the stages remained stationary. The grooved substrate surface is caused by the manual polishing process (Methods). **b**, Diagram of the measured linewidths (blue dots, left vertical axis) and measured line heights (red crosses, right vertical axis) versus the projected linewidth in units of pixels (bottom horizontal axis) or micrometres (top horizontal axis). The small dots (crosses) represent individual measurements and the large dots (crosses) indicate the average width (height). The measured linewidth increases monotonically with the projected width. The height increases monotonically and plateaus at a height of about 4 µm, which can be explained by the finite width of the incident light-sheet beam. We consider the encircled data points as the minimal reproducibly attainable voxel sizes.

data. Again, the data describe a sigmoid shape for all wavelengths λ_2 in the probed range. The solid curves are derived from fitting logistic functions to the measured data. The sigmoid midpoints are highlighted by a large dot and connected by a black curve. We expect the sigmoid's midpoint location to correlate with the intermediate-state absorbance at the respective wavelength. Indeed, the two-colour two-step absorption character of biacetyl is confirmed by the black curve, that is, the action spectrum[36], which contains the characteristic minima and maxima of the extinction spectrum[26] (Fig. 2c, right). The detailed shapes of extinction and action spectra do not agree though, which points to not-well-understood aspects of photopolymerization in many systems beyond two-colour two-step absorption[36].

Light-sheet 3D printing setup

We now turn our attention to the actual light-sheet 3D printing experiments. For this purpose, a separate, dedicated setup was built. A diagram of the setup employed for light-sheet 3D printing is shown in Fig. 3a. It consists of two laser beam paths: one is the stationary red-light-sheet beam and the other one projects slices of the object using blue light. Both beams cross each other inside a cuboid cuvette chamber, which is mounted on a thin glass coverslip (Methods). The projection beam path consists of four multimode laser diodes. As evident from the emission spectra (Supplementary Fig. 3), the measured emission wavelengths scatter at around 440 nm. The diode's spatial emission profiles are homogenized through a rectangular-core glass fibre. The fibre end facet is imaged onto a 720 Hz frame rate, high-definition liquid-crystal display (LCD), which is imaged through a long-working-distance, high-NA microscope objective lens into the cuvette. For the light-sheet beam, a 660 nm laser beam is shaped using a Powell lens into a line-shaped beam. This beam is then focused into the cuvette by a second microscope lens with low NA. Supplementary Notes 2 and 3 discuss the results of the light-sheet beam and projection beam characterization.

A photograph of the mounted photoresin cuvette is shown in Fig. 3b. A glass rod of 1 mm diameter is dipped into the photoresin and the two objective lenses are focused onto the polished glass rod's end facet, which serves as the 3D printing substrate. The glass rod is mounted on a set of precision translation stages (not depicted), including a low-inertia piezo-stage. By printing on a movable substrate, the printed structure dimensions are not limited by the field of view of the projected image. After printing, all the structures are developed for 30 s in acetone, with the exception of line gratings, which are supercritically dried in CO_2. In contrast to many other optical 3D printing methods, no laborious post-exposure UV illumination or other post-processing is necessary.

Voxel size and 3D printing rate

We determine the attainable minimum feature sizes of our light-sheet 3D printer by printing suspended line gratings with a length of 20 µm, pitch of 6 µm and fixed blue-laser exposure time of 5 ms (Fig. 4a). For this experiment, the red laser power is set to $P_2 = 3$ W, leading to a peak intensity of 3 mW µm^{-2}. The blue laser intensity in the focal plane is $I_1 = 162\ \mu W\ \mu m^{-2}$. A plot of the measured linewidths versus the designed linewidths is shown in Fig. 4b. The smaller pale symbols indicate individual measurements, and the larger symbols are average values. The minimum reproducibly attainable linewidth and hence the voxel diameter is $d_{voxel} = 0.5$ µm, obtained for a projected linewidth of 9 pixels. However, the targeted linewidth in this case is 0.75 µm and hence larger. The ratio of targeted linewidth and measured linewidth decreases for wider lines. We attribute the deviation between attained and targeted linewidths to three aspects. First, the limited modulation transfer function of the projection system smears out the ideally rectangular illumination profiles (Supplementary Fig. 17). This rounding of exposure together with a threshold behaviour of the photoresin leads to a reduced linewidth. Second, before the monomer is crosslinked, quenchers and scavengers within the printing volume must be depleted[37,38]. The depletion process proceeds faster in the centre of the printing volume than in the periphery, where the concentration of quenchers and scavengers is restored by an in-diffusion process from the unexposed surrounding (Supplementary Note 1). Third, polymer shrinkage may also contribute to the attained smaller linewidth. The corresponding line height is plotted on the right vertical scale (Fig. 4b). Evidently, a height of $h_{voxel} = 2.2$ µm is reproducibly achieved, resulting in a voxel aspect ratio of $h_{voxel}/d_{voxel} = 4.4$. We emphasize that it is possible to print even thinner lines. However, 32% of the six-pixel-wide lines broke during printing or development, which is contrasted by the 100% yield for the nine-pixel-wide lines. Hence, in the spirit of making conservative claims, we do not quote these values.

On this basis, we derive the total peak voxel printing rate[13]. This metric allows for comparing different 3D printing approaches, which can have vastly different voxel volumes, in a meaningful manner[13]. The LCD has a resolution of 1,920 × 1,080 pixels, equivalent to a total of 2.07×10^6 pixels. This value corresponds to 3.3×10^4 voxels with the above voxel diameter of 9 pixels (assuming a round voxel shape). For an exposure time of 5 ms, as used for the printing of line gratings, we obtain a voxel printing rate of 7×10^6 voxels s^{-1} at a voxel volume of $(0.5\ \mu m)^2 \times 2.2\ \mu m = 0.55\ \mu m^3$ and thus to a volume printing rate of $3.85 \times 10^6\ \mu m^3\ s^{-1}$. These values are compared with other 3D printing methods (Supplementary Fig. 20).

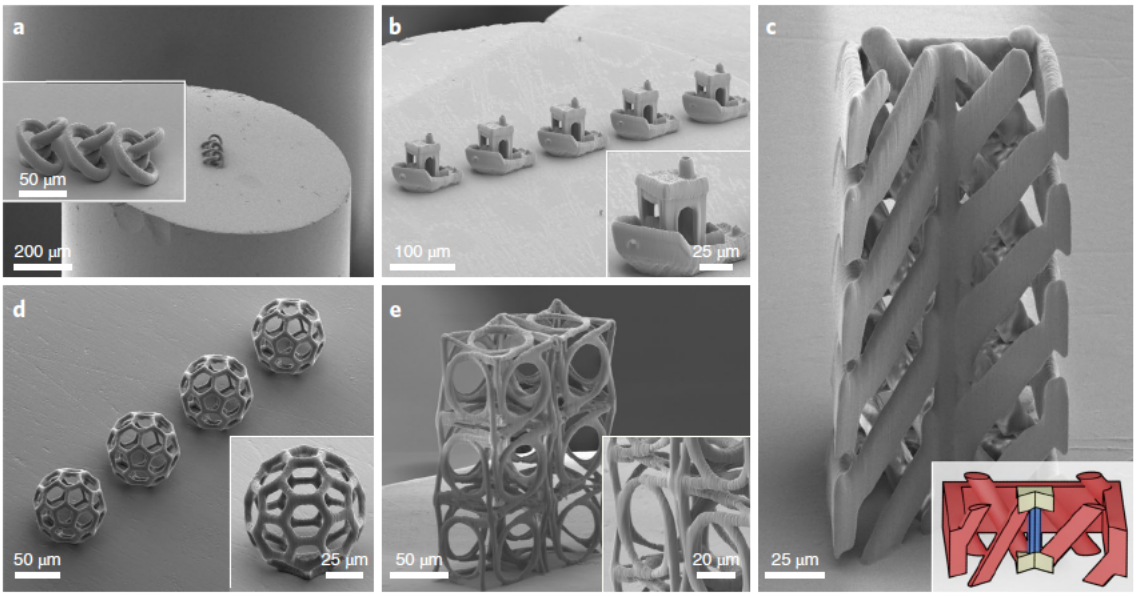

Fig. 5 | Oblique-view SEM images of light-sheet 3D printed micro-objects. **a**, Knot-like structures printed on an intentionally slanted borosilicate glass rod. Three structures were printed in parallel. **b**, A small fleet of #3DBenchy structures. The inset reveals that overhanging features and holes are reproduced. The individual boats were sequentially printed by stitching several printing fields. **c**, Five stacked unit cells of a mechanical metamaterial, which was designed to obtain a roton-like acoustical-wave dispersion relation[39]. The inset shows the rendering of a single unit cell from the same perspective. The large overhanging and flying features make this structure notoriously challenging to 3D print using laser-focus-scanning two-photon printing[29]. A flyby SEM video is provided in the Supplementary Information. **d**, Buckyball structures with a diameter of 80 µm, sequentially printed by stitching several writing fields. **e**, Six chiral metamaterial unit cells[40]. The inset reveals that the rings on the side walls are well separated from the adjacent vertically lying rings. The printing time per unit cell is 117 ms and hence more than ten times shorter compared with the results from a previous work employing laser-focus-scanning two-photon 3D nanoprinting[13]. All the 3D structures were printed at ~350 µm s^{-1} substrate *z* velocity and blue-laser peak intensities of $I_1 = 22$ µW $µm^{-2}$. Real-time videos of the 3D printing process are available in the Supplementary Information.

Light-sheet 3D printed structures

Scanning electron microscopy (SEM) images of 3D printed structures are shown in Fig. 5. We used the highly viscous photoresin PR3 for all the light-sheet 3D printed structures, since highly viscous multifunctional acrylates were found to have a long 'intrinsic polymerization time constant' and hence little change in refractive index occurs during the exposure phase[38]. Therefore, scattering effects of the light-sheet at already polymerized parts are kept low. Figure 5a shows three knot-like structures, which were printed in parallel within 153 ms. Figure 5b shows a fleet of five #3DBenchy boats (https://www.3dbenchy.com/), which are a well-established benchmark structure in the community of 3D additive manufacturing. Each boat was printed within one printing field and took 266 ms to be printed. The boat's hulls has a 100% filling fraction, resulting in proximity effects in the subsequent layers, that is, the boat's window. To pre-compensate the proximity effect, we use a greyscale exposure profile, thus lowering the blue laser intensity in volumes with high local filling fraction (Supplementary Methods and Supplementary Fig. 19). In Fig. 5c, five quarter-cut acoustic metamaterial unit cells are printed on top of each other. This metamaterial was previously designed to yield a roton-like acoustic dispersion relation[39]. The structure is especially challenging in fabrication using laser-scanning two-photon 3D microprinting: the outer walls are only fixed at two edges during printing, causing parts of the structure to drift off in the photoresin. For light-sheet 3D microprinting, this problem is absent, since each unit cell is printed within 117 ms. The entire stack is completed within 583 ms. The striped pattern on the structure's surface is most probably the result of speckles arising from the blue beam path. The buckyballs (Fig. 5d) allow for a comparison with other 3D printing approaches[17,20]. Each ball was printed within 250 ms. Finally, the chiral metamaterial[40] (Fig. 5e) has a footprint width of 155 µm, spanning almost the entire field of view. Despite the inhomogeneities observed in the light-sheet characterization (Supplementary Fig. 14), no irregularities are observed in the structure quality. Furthermore, the lattice constant of 77 µm is similar to our previously published study[13]. There, the printing time per unit cell was 1.6 s. Using light-sheet 3D microprinting, two unit cells were printed within 233 ms, that is, 117 ms per unit cell—a speedup of more than tenfold, although at a lower resolution. These structures prove that the presented photoresin and 3D printing setup are well suited for the fast production of 3D microstructures. However, we note that printing larger overall structures is still challenging for the used photoresin due to the gradual dose accumulation at the bottom of the photoresin vat, eventually leading to an impaired optical resolution for the projected layer.

Discussion and conclusion

Herein, we have demonstrated light-sheet 3D microprinting with voxel volumes of 0.55 $µm^3$ and peak voxel printing rates of 7×10^6 voxels s^{-1}. This major advance was enabled by a suitable photoinitiator system, composed of the two-colour two-step initiator biacetyl and TEMPO (serving as both quencher and scavenger). An in-depth analysis of the underlying mechanisms has been presented, including a rate model analysis of the polymerization process. We have showcased the 3D printing capabilities of this photoinitiator system using a dedicated light-sheet 3D printing setup, containing a red and blue continuous-wave laser source. Also, 3D printing jobs were completed in a fraction of a second.

Altogether, P. V. Braun and M. L. Brongersma[41] were accurate when writing about two-step absorption in 2021: 'where this approach has real potential to shine is in the scalability of the process'. Using light-sheet 3D printing, the print time per part has now come close to typical manufacturing times in injection moulding. However, for the widespread use of light-sheet 3D microprinting, three aspects

need further improvement. First, the total sample fabrication time is presently dominated by sample handling, that is, print setup, sample transport and development. These steps can be automated, for example, by using microfluidics[42], or by automatically immersing the sample in liquid containers[43]. Second, the photoresin as presented here limits the total exposed volume. After prolonged printing, out-of-focus areas polymerize due to proximity effects. Such accumulation or depletion effects can likely be suppressed by using further improved photoresin formulations. Directions for optimization can be deduced from the rate model analysis presented here. In addition, the in situ replenishment of the used photoresin by using microfluidics, polymerization inhibition by an oxygen-permeable membrane (as used in CLIP[8]), or volumetric polymerization inhibition patterning[10] can potentially further suppress out-of-focus polymerization. Third, the red solid-state laser can be replaced by inexpensive high-power laser diodes, as is already the case for the blue laser. Compared with the amplified femtosecond pulsed lasers used in FP-TPL, the continuous-wave lasers used in this work are already much less expensive and easier to operate. The development of two-colour two-step photoinitiators improved with respect to sensitivity and tuned to readily available laser wavelengths would be highly desirable for this aspect.

The underlying logical-AND-type functionality is not limited to light-sheet 3D printing, but could also prove beneficial in combination with CAL[5–7], where a two-colour projection system was recently demonstrated for multimaterial 3D printing[44]. Related CAL setups could be used to simultaneously expose the photoresin using two-colour two-step absorption, with the two colours impinging from different directions, thereby reducing the proximity effect and voxel size.

Online content

Any methods, additional references, Nature Research reporting summaries, source data, extended data, supplementary information, acknowledgements, peer review information; details of author contributions and competing interests; and statements of data and code availability are available at https://doi.org/10.1038/s41566-022-01081-0.

References

1. Fassi, I. & Shipley, D. *Micro-Manufacturing Technologies and Their Applications: A Theoretical and Practical Guide* (Springer International Publishing, 2017).
2. Ngo, T. D., Kashani, A., Imbalzano, G., Nguyen, K. T. Q. & Hui, D. Additive manufacturing (3D printing): a review of materials, methods, applications and challenges. *Compos. B Eng.* **143**, 172–196 (2018).
3. Zheng, X. et al. Ultralight, ultrastiff mechanical metamaterials. *Science* **344**, 1373–1377 (2014).
4. Zheng, X. et al. Multiscale metallic metamaterials. *Nat. Mater.* **15**, 1100–1106 (2016).
5. Shusteff, M. et al. One-step volumetric additive manufacturing of complex polymer structures. *Sci. Adv.* **3**, eaao5496 (2017).
6. Kelly, B. E. et al. Volumetric additive manufacturing via tomographic reconstruction. *Science* **363**, 1075–1079 (2019).
7. Loterie, D., Delrot, P. & Moser, C. High-resolution tomographic volumetric additive manufacturing. *Nat. Commun.* **11**, 852 (2020).
8. Tumbleston, J. R. et al. Continuous liquid interface production of 3D objects. *Science* **347**, 1349–1352 (2015).
9. Walker, D. A., Hedrick, J. L. & Mirkin, C. A. Rapid, large-volume, thermally controlled 3D printing using a mobile liquid interface. *Science* **366**, 360–364 (2019).
10. Beer, M. P. de et al. Rapid, continuous additive manufacturing by volumetric polymerization inhibition patterning. *Sci. Adv.* **5**, eaau8723 (2019).
11. Kato, J., Takeyasu, N., Adachi, Y., Sun, H.-B. & Kawata, S. Multiple-spot parallel processing for laser micronanofabrication. *Appl. Phys. Lett.* **86**, 044102 (2005).
12. Matsuo, S., Juodkazis, S. & Misawa, H. Femtosecond laser microfabrication of periodic structures using a microlens array. *Appl. Phys. A* **80**, 683–685 (2005).
13. Hahn, V. et al. Rapid assembly of small materials building blocks (voxels) into large functional 3D metamaterials. *Adv. Funct. Mater.* **30**, 1907795 (2020).
14. Saha, S. K. et al. Scalable submicrometer additive manufacturing. *Science* **366**, 105–109 (2019).
15. Somers, P. et al. Rapid, continuous projection multi-photon 3D printing enabled by spatiotemporal focusing of femtosecond pulses. *Light Sci. Appl.* **10**, 199 (2021).
16. Hahn, V., Mayer, F., Thiel, M. & Wegener, M. 3-D laser nanoprinting. *Opt. Photonics News* **30**, 28–35 (2019).
17. Regehly, M. et al. Xolography for linear volumetric 3D printing. *Nature* **588**, 620–624 (2020).
18. Oron, D., Tal, E. & Silberberg, Y. Scanningless depth-resolved microscopy. *Opt. Express* **13**, 1468–1476 (2005).
19. Tal, E., Oron, D. & Silberberg, Y. Improved depth resolution in video-rate line-scanning multiphoton microscopy using temporal focusing. *Opt. Lett.* **30**, 1686–1688 (2005).
20. Hahn, V. et al. Two-step absorption instead of two-photon absorption in 3D nanoprinting. *Nat. Photon.* **15**, 932–938 (2021).
21. Bäckström, H. L. J., Sandros, K., Lindgren, J.-E., Varde, E. & Westin, G. Transfer of triplet state energy in fluid solutions. I. Sensitized phosphorescence and its application to the determination of triplet state lifetimes. *Acta Chem. Scand.* **14**, 48–62 (1960).
22. Lewis, G. N. & Kasha, M. Phosphorescence and the triplet state. *J. Am. Chem. Soc.* **66**, 2100–2116 (1944).
23. Sidman, J. W. & McClure, D. S. Electronic and vibrational states of biacetyl and biacetyl-d_6 I. Electronic states. *J. Am. Chem. Soc.* **77**, 6461–6470 (1955).
24. Bäckström, H. L. J. & Sandros, K. The quenching of the long-lived fluorescence of biacetyl in solutions. *Acta Chem. Scand.* **12**, 823–832 (1958).
25. Green, W. A. *Industrial Photoinitiators: A Technical Guide* (CRC Press, 2010).
26. Singh, A., Scott, A. R. & Sopchyshyn, F. Flash photolysis of camphorquinone and biacetyl. *J. Phys. Chem.* **73**, 2633–2643 (1969).
27. Almgren, M. The natural phosphorescence lifetime of biacetyl and benzil in fluid solution. *Photochem. Photobiol.* **6**, 829–840 (1967).
28. Taylor, R. P. & Blacet, F. E. Photochemical oxidation of biacetyl by molecular oxygen. *Ind. Eng. Chem.* **48**, 1505–1508 (1956).
29. Padnos, N. & Noyes, W. A. Photolysis of biacetyl-oxygen mixtures at 4358 Å. *J. Phys. Chem.* **68**, 464–468 (1964).
30. Schwerzel, R. E. & Caldwell, R. A. Quenching of excited states by stable free radicals. II. Mechanism of triplet quenching by di-*tert*-butyl nitroxide. *J. Am. Chem. Soc.* **95**, 1382–1389 (1973).
31. Lissi, E. A. & Encina, M. V. Polymerization photosensitized by carbonyl compounds. *J. Polym. Sci. Polym. Chem. Ed.* **17**, 2791–2803 (1979).
32. Concheanainn, C. O. & Sidebottom, H. W. Temperature dependence of the triplet lifetime of biacetyl in the gas phase. *J. Photochem.* **13**, 55–66 (1980).
33. Sawaki, Y. Mechanistic study on the photo-oxidation of α-diketones: interaction of triplet α-diketones with oxygen. *Tetrahedron* **41**, 2199–2205 (1985).
34. Likhtenshtein, G. I. *Nitroxides Brief History, Fundamentals, and Recent Developments* (Springer Nature, 2020).
35. Gijsman, P. A review on the mechanism of action and applicability of hindered amine stabilizers. *Polym. Degrad. Stab.* **145**, 2–10 (2017).

36. Irshadeen, I. M. et al. Action plots in action: in-depth insights into photochemical reactivity. *J. Am. Chem. Soc.* **143**, 21113–21126 (2021).
37. Decker, C. & Jenkins, A. D. Kinetic approach of oxygen inhibition in ultraviolet- and laser-induced polymerizations. *Macromolecules* **18**, 1241–1244 (1985).
38. Mueller, J. B., Fischer, J., Mayer, F., Kadic, M. & Wegener, M. Polymerization kinetics in three-dimensional direct laser writing. *Adv. Mater.* **26**, 6566–6571 (2014).
39. Chen, Y., Kadic, M. & Wegener, M. Roton-like acoustical dispersion relations in 3D metamaterials. *Nat. Commun.* **12**, 3278 (2021).
40. Frenzel, T., Kadic, M. & Wegener, M. Three-dimensional mechanical metamaterials with a twist. *Science* **358**, 1072–1074 (2017).
41. Braun, P. V. & Brongersma, M. L. Photochemistry democratizes 3D nanoprinting. *Nat. Photon.* **15**, 871–873 (2021).
42. Mayer, F. et al. Multimaterial 3D laser microprinting using an integrated microfluidic system. *Sci. Adv.* **5**, eaau9160 (2019).
43. Maruyama, T., Hirata, H., Furukawa, T. & Maruo, S. Multi-material microstereolithography using a palette with multicolor photocurable resins. *Opt. Mater. Express* **10**, 2522–2532 (2020).
44. Wang, B. et al. Stiffness control in dual color tomographic volumetric 3D printing. *Nat. Commun.* **13**, 367 (2022).
45. Hanemann, T. & Honnef, K. Optical and thermomechanical properties of doped polyfunctional acrylate copolymers. *Polymers* **10**, 337 (2018).
46. Porter, G. B. Photooxidation of biacetyl. *J. Chem. Phys.* **32**, 1587–1588 (1960).
47. Bensasson, R. & Land, E. J. Triplet-triplet extinction coefficients via energy transfer. *Trans. Faraday Soc.* **67**, 1904–1915 (1971).

Methods

Point-scanning printing setup

The point-scanning printing setup consists of a laser emitting at 440 nm wavelength (LDH D-C-440, Picoquant). To clean the spatial laser mode, the emitted radiation is coupled into a single-mode polarization-maintaining optical fibre (PMC-400Si-2.3-NA014 3-APC-300-P, Schäfter+Kirchhoff). An acousto-optical modulator (MT80-1.5-400.442, AA Opto Electronic) is used for modulating the outcoupled beam power (60SMS-1-4-M12-33, Schäfter+Kirchhoff). The beam of the laser is combined with the collimated beam of a 640 nm wavelength fibre-coupled laser (iBeam smart PT-640, TOPTICA Photonics) by a dichroic mirror (DMLP567, Thorlabs). The emission spectra of the lasers emitting at 440 and 640 nm are provided in Supplementary Figs. 1 and 2, respectively. The combined beams are reflected by a polarizing beam combiner cube (PBS251, Thorlabs) and deflected by a pair of galvanometer mirrors (Saturn 5B 56S, Pangolin Laser Systems). The galvanometer mirrors are imaged by a Keplerian telescope, consisting of two achromatic lenses (ACL254-100-A and ACL254-150-A, Thorlabs) into the rear aperture of the microscope objective lens (HCX PL APO 100×/1.4–0.7 OIL CS, Leica Microsystems), which is mounted on an inverted microscope mount (DM IRB, Leica Microsystems). The objective lens focuses the combined laser beams through the immersion oil (Type F, Leica Microsystems) and the glass coverslip substrate (no. 1.5H, Paul Marienfeld) into the liquid photoresin sample. The photoresin (25 µl) is contained in a 5-mm-diameter polydimethylsiloxane ring, which is sealed from the top with a second coverslip to suppress the evaporation of biacetyl during extended printing experiments. Before printing, the substrates are cleaned in a solution of Hellmanex III (Hellma) and silanized with 3-(trimethoxysilyl)propyl methacrylate (Merck). The sample cell is mounted in a 3D piezo-stage (P-527.3CL, Physik Instrumente), which, in turn, is mounted on a motorized stage (Scan IM 120 × 100, Märzhäuser Wetzlar).

For the experiments shown in Supplementary Fig. 6, a 405 nm wavelength laser diode (L405P150, Thorlabs) is used as the blue laser beam. The diode is mounted in a temperature-controlled mount (LDM56/M, Thorlabs). The temperature is controlled by a thermoelectric cooler controller (TED200C, Thorlabs). The diode is first collimated by an aspheric lens (A240TM-A, Thorlabs) and then focused by a 40-mm-focal-length plano-convex lens (LA1422-A, Thorlabs) through a 10-µm-diameter pinhole (P10C, Thorlabs). The focused beam is collimated again by a 75-mm-focal-length achromat (AC254-075-A, Thorlabs) and then combined with the red beam path.

For the experiments at 685 and 660 nm wavelengths (Fig. 2c), the beam of the 640 nm laser is replaced by the collimated beam of red laser diodes (HL6750MG and HL6545MG, respectively; Thorlabs). Therefore, the laser diodes are mounted in the temperature-controlled mount (LDM56/M, Thorlabs), whose temperature is controlled by a thermoelectric cooler controller (TED200C, Thorlabs). To cover the wavelength range greater than 700 nm (Fig. 2c), a Ti:Sa laser (MaiTai HP, Newport Spectra-Physics) is used in a non-mode-locked mode, that is, at low pump power and with a switched-off intracavity acousto-optical modulator. An (extra-cavity) acousto-optical modulator (MTS-40-A3-750.850, AA Opto Electronics) modulates the laser beam power. The Ti:Sa laser beam is then combined with the other laser beams by the polarizing beam combiner cube.

All the laser beams are expanded using Keplerian telescopes such that they overfill the entrance pupil of the objective lens. The laser beam foci are superimposed in the focal plane and characterized with the aid of the reflected signal of gold beads (80 nm nominal diameter) dispersed on a glass coverslip and embedded in an optical adhesive. The laser powers are measured using a semiconductor power sensor (TP86, Coherent).

Light-sheet 3D printing setup

For substrate positioning, four stages are used: L306 for positioning in the *z* direction, two voice-coil stages V528.1AA for positioning in the *x* and *y* direction, and a piezo-stage P622.ZCD for fast scanning in the *z* direction (all the stages are from Physik Instrumente). The stages are mounted hanging on a breadboard above the optical table.

For the projection beam path, four 6 W optical-power, 440 nm wavelength laser diodes (PD-01231, Lasertack) are coupled into a rectangular-core optical fibre (NA = 0.22; core dimensions, 810 × 405 µm^2; fibre length, 1 m; Ceramoptec). The four laser diodes aid in suppressing the speckle patterns generated by the optical fibre. An emission spectrum is provided in Supplementary Fig. 3. The fibre end facet is imaged by a Keplerian telescope, consisting of a Zeiss EC Epiplan-Neofluar 20×/0.5 objective and an achromat with a focal length of 150 mm. Thereafter, the initially unpolarized beam passes a polarizing beamsplitter (using the transmitted beam; model PBS251, Thorlabs), a half-wave plate (WPH10M-445, Thorlabs), a second polarizing beamsplitter (using the reflected beam; model PBS251, Thorlabs) and a quarter-wave plate (WPQ10M, Thorlabs). The image of the fibre's end facet is directed onto the reflective LCD (active area, 12.5 × 7.1 mm^2; display resolution, 1,920 × 1,080 pixels; frame rate, 720 Hz; model HED4552, Holoeye). For the presented light-sheet 3D printer, LCDs are advantageous to digital micromirror devices (DMDs) for two reasons. First, the (possibly non-uniform) micromirror tilt-angle variance in DMDs impedes the design of projection systems in which the DMD is highly demagnified. Second, LCDs natively support greyscale intensity modulation (Supplementary Methods), whereas DMDs display binary intensity patterns and hence achieve greyscale modulation by temporally averaging over multiple frames. Nevertheless, it is conceivable that a 3D light-sheet laser printer could also be built using a DMD. At the LCD, the incident beam is circularly polarized. The handedness of the circular polarization is reversed on reflection off nominally white pixels, whereas the handedness of light incident on nominally black pixels is preserved on reflection. The reflected light passes the quarter-wave plate again, converting the circular polarization to linear polarization with perpendicular polarization axes for light reflected off white and black pixels. The second polarizing beamsplitter now transmits light reflected off the white pixels. After the polarizing beamsplitter, we measured a contrast of the intensities of white and black pixels of 314. A tube lens (ITL200, Thorlabs) images the LCD plane to infinity with the tube lens' exit pupil located at the entrance pupil of the long-working-distance microscope objective lens (LD LCI Plan-Apochromat 63×/1.2 Imm Corr DIC, Carl Zeiss). At the entrance pupil of the objective lens, the beam is linearly polarized along the *y* direction. The objective lens tightly focuses the beam through a thin layer of immersion fluid (Zeiss Immersol 518F) into the photoresin vat. A ray-traced optical path diagram of the projection path is shown in Supplementary Fig. 16. The corresponding calculations of the point spread function are shown in Supplementary Fig. 17.

The photoresin vat consists of a thin coverslip (CG00C, Thorlabs) glued on a 5 mm cut piece of a UV-transparent plastic cuvette (BRAND). The photoresin vat is mounted on manual goniometric and linear stages.

The light-sheet beam is generated by focusing the beam of a 6 W optical-power, 660 nm wavelength solid-state laser (axiom, Laser Quantum) by a Powell lens (1° fan angle, optimized for 1 mm beam diameter; model LOCP-8.9R01-1.0, Laserline Optics Canada). The laser's emission spectrum is shown in Supplementary Fig. 4. The beam is collimated by a set of spherical and cylindrical lenses (LA1131-A-ML, LJ1629RM-A and LJ1267RM-A, Thorlabs) before it is focused into the sample vat by a microscope objective lens (Epiplan 5×/0.13, Carl Zeiss). The light-sheet beam is linearly polarized in the *y* direction and thus impinges in the transverse-electric polarization onto the substrate.

The substrates are 1 mm in diameter. The glass rods (Hilgenberg) are cut to a length of 13 mm and manually polished. For aligning the plane of the light-sheet beam to be parallel to the focal plane of the microscope objective lens, the glass rod's end facet is polished to an angle of 45°. The reflected light of the light-sheet beam is collected by the high-NA

objective lens and imaged on a camera, which is mounted on the idle port of the second polarizing beamsplitter. For 3D printing, the end facet is polished to an angle of 8° to suppress the standing-wave pattern generated by the grazing-incidence light-sheet beam (Supplementary Fig. 15).

The LCD is controlled by a dedicated controller board (Holoeye) that receives an HDMI signal containing a colour-video stream at a frame rate of 60 Hz and 4K resolution (3,840 × 2,160 pixels). Each 4K colour frame is decoded into 12 full-high-definition (1,920 × 1,080 pixels) greyscale images. The 4K stream is sent by a graphics processing unit (NVIDIA GeForce GTX 970), which is part of a personal computer, running on a stock Debian GNU/Linux operating system. A single program written in C++14 synchronizes the direct video output, laser power modulation and stage movement with sufficient precision despite the underlying pre-emptive scheduler of the operating system.

Sample development

The development procedure for the point-scanning experiments is described elsewhere[20]. The light-sheet 3D printed structures are developed for 30 s in acetone, except for the line-grating structures, which were supercritically dried in CO_2 (EM CPD300, Leica Microsystems). Neither post-printing UV flood illumination nor any other post-processing was performed (in contrast to other works[15,17]). The residual photoresin is removed from the cuvette in a bath of spectroscopy-grade isopropanol (15 min). After several runs, the cuvette is cleaned in a 2 vol% solution of Hellmanex III (Hellma) at 50 °C temperature.

Sample characterization

All the point-scanning samples are characterized as that done elsewhere[20]. The samples are imaged in an upright microscope (DMLM, Leica Microsystems) using a 0.9 NA objective lens (N Plan 100×) in the reflection dark-field mode onto a camera sensor (EOS 70D, Canon).

The samples of the light-sheet 3D printing setup are imaged in a digital microscope (Smartzoom 5, Carl Zeiss) and SEM instrument (Supra 55VP, Carl Zeiss). For the SEM images, the primary electron energy is 5 kV.

Data availability

The data underlying the plots in this paper and its Supplementary Information and the related 3D printing files are available via the open-access data repository of the Karlsruhe Institute of Technology (https://doi.org/10.5445/IR/1000150926).

Acknowledgements

We acknowledge fruitful discussions with P. Jöckle and A. Neil-Unterreiner (both from the Institute of Physical Chemistry, KIT). We thank R. Batchelor and M. Nardi (both formerly at the ITCP, KIT) for synthesizing, purifying and analysing the chemicals related to the project. We thank M. A. Seiberlich (Light Technology Institute, KIT) for funded by the Max Planck School of Photonics. This research has additionally been funded by the Deutsche Forschungsgemeinschaft (DFG, German Research Foundation) under Germany's Excellence Strategy via the Excellence Cluster '3D Matter Made to Order' (EXC-2082/1-390761711), which has also been supported by the Carl Zeiss Foundation through the 'Carl-Zeiss-Foundation-Focus@HEiKA', by the State of Baden-Württemberg and by KIT. We further acknowledge support by the Helmholtz program 'Materials Systems Engineering' (MSE), the Karlsruhe School of Optics & Photonics (KSOP), and the Ministry of Science, Research and Arts of Baden-Württemberg as part of the sustainability financing of the projects of the Excellence Initiative II. C.B.-K. acknowledges funding via an Australian Research Council (ARC) Laureate Fellowship enabling his photochemical research program (FL170100014).

Author contributions

V.H. proposed the idea for light-sheet 3D printing using two-colour two-step absorption to M.W. V.H. and E.B. searched the literature for suitable photoinitiator candidates, including suggestions from C.B.-K. V.H. and P.M. experimentally screened the photoinitiator candidates. V.H. searched the literature for quenchers and scavengers and characterized the photoresins. P.R. characterized the photoresins in argon and oxygen atmospheres. T.S. and W.W. calculated the molecular electronic transitions of biacetyl. V.H. designed the light-sheet 3D printing setup. F.H. set up and programmed the control unit for the LCD and the stages. M.W. supervised the project. All the authors participated in the discussions on the project. V.H. and M.W. drafted an initial version of the manuscript. All the authors contributed to the interpretation of the results and to the writing of the manuscript.

Competing interests

V.H., P.M., E.B. and M.W. are inventors on a patent application filed in Germany on light-sheet 3D printing (DE102018009916A1). The other authors declare no competing interests.

Additional information

Supplementary information The online version contains supplementary material available at https://doi.org/10.1038/s41566-022-01081-0.

Correspondence and requests for materials should be addressed to Vincent Hahn.